https://doi.org/10.5194/essd-2025-583
Preprint. Discussion started: 12 November 2025

Global Surface Mining and Land Reclamation of Time Series from 1985–2022

Sucheng Xu [a,1], Jiatong Zhou [a,1], Kechao Wang [a], Stefan Giljum [c], Victor Maus [c,d], Tim T. Werner [e], Liang Tang [f], Jiwang Guo [a],Wu Xiao [a,b,*]

a School of Public Affairs, Zhejiang University, Hangzhou, China.
b Land Academy for National Development, Zhejiang University, Hangzhou, China.
c Institute for Ecological Economics, Vienna University of Economics and Business (WU), Vienna, Austria.
d Novel Data Ecosystems for Sustainability Research Group, Advancing Systems Analysis, International Institute for Applied Systems Analysis (IIASA), Laxenburg, Austria.
e School of Geography, Earth and Atmospheric Sciences, University of Melbourne, 221 Bouverie Street, Carlton, VIC, 3010, Australia.
f College of Earth and Planetary Sciences, Chengdu University of Technology, 610059 Chengdu, China.

Abstract: Surface mining has profound impacts on ecosystems, contributing to land degradation, vegetation loss, pollution, and threats to biodiversity. Given the rapidly rising demand for raw materials, understanding the dynamics of mining and reclamation processes is essential to support sustainable development. Here, we integrate and analyze a large set of mines distributed worldwide based on their known land extent circa year 2020. We integrated time-series data of the Normalized Difference Vegetation Index (NDVI), nighttime light (NTL) intensity, and land use to detect and identify changes within mine sites from 1985 to 2022 and assess spatiotemporal trajectories of mining and reclamation processes. The dataset comprises 74,726 polygons, covering a total area of 82,552 km^2. Our dataset obtained the maximum potential mining disturbance boundary—the cumulative outer envelope of mining-induced land disturbance over the study period. China leads in both the number and the areal extent of mining sites, followed by the United States and Australia. Within the analyzed set of polygons, mining land footprint expanded steadily between 1985 and 2022, with the annual disturbed area peaking at 1,943 km^2 in 2015, with a slowing expansion after 2015. From 1985 to 2022, the cumulative area of land converted to mine reached 40,596 km^2, accounting for 49 % of the total surface mining area in our set, while the reclaimed area was 29,285 km^2. Active mining areas dominated the global mining landscape, comprising 31.6 % of all polygons, with approximately 48.9 % concentrated in Asia. The spatiotemporal processes and patterns revealed in this study provide crucial insights into the development of mine sites and provide new data to support ecological impact assessments and sustainable development research in global

---
[1] *These authors contributed equally to this work.*
[*] *Corresponding author: Wu Xiao, xiaowu@zju.edu.cn.*

https://doi.org/10.5194/essd-2025-583
Preprint. Discussion started: 12 November 2025

Earth System Science Data Discussions
Open Access

mining regions.

Keywords: Global surface mining; spatiotemporal variation; Mining areas;

1 Introduction

Mining activities are a fundamental driver of global economic growth and play a key role in industrial development (Pavloudakis et al., 2024). However, mining causes significant disruptions to ecosystems, particularly through vegetation loss, biodiversity decline, water pollution and ecological degradation (Chen et al., 2025b; Giam et al., 2018; Giljum et al., 2025; Qian et al., 2018; Xiang et al., 2021). Surface mining, involving extensive soil stripping and land excavation, alters the surface landscape, significantly modifies ecosystem structure and function, and causes habitat loss, which contributes to biodiversity decline (Firozjaei et al., 2021; Giljum et al., 2022; Ma et al., 2021; Xiao et al., 2020a; Yan et al., 2024; Zhao et al., 2023). Studies in tropical regions, for example, have shown that mining activities can cause deforestation within a 70 km radius, with indirect impact up to 28 times greater than direct impacts (Ladewig et al., 2024; Sonter et al., 2017). As global demand for mineral resources continues to grow, mining activities have expanded at an unprecedented rate. Global production of mineral fuels, metal ores, and industrial minerals increased by 66 % over the past two decades, reaching almost 80 billion tons by 2024 (UNEP IRP, 2024). The International Energy Agency (IEA) estimates that achieving net-zero global greenhouse gas emissions by 2050 will require a sixfold increase in demand for key minerals, with some critical minerals, such as lithium, experiencing a 40-fold increase (Carr-Wilson et al., 2024). As the scale of mining inevitably expands globally, the need for monitoring and assessing its ecological impacts is becoming increasingly urgent. A systematic understanding and analysis of the precise spatial locations of global mining activities, the boundaries of mining-induced degradation, and reclamation processes form the foundation for assessing the ecological impacts of mining. However, impacts on more than half of the world’s mining areas go unrecorded due to data limitations (Maus and Werner, 2024), severely limiting the precise assessment of mining’s environmental impact and the exploration of sustainable development pathways.

Globally, research focused on delineating mining area boundaries and monitoring the spatiotemporal dynamics of vegetation disturbance and reclamation is steadily increasing (Werner et al., 2019). However, these studies still have considerable room for improvement, particularly regarding the number of mining sites, boundary accuracy, and monitoring methods for vegetation disturbance. In recent years, visual interpretation of satellite imagery has been applied to studies on delineating mining area boundaries (Murguía and Bringezu, 2016). Werner et al. (2020) utilized satellite data to directly map 295 major mine sites globally, focusing on delineating and classifying each specific mine feature in high spatial detail, shifting the focus from broader affected regions to the operational footprints themselves. On a global scale, Maus et al. (2020) manually delineated 21,060 mining polygons, totalling 57,277 km^2, by visual interpretation of satellite images, focusing on 10 km buffers around the approximate

https://doi.org/10.5194/essd-2025-583
Preprint. Discussion started: 12 November 2025

coordinates of over 6,000 active mining sites across the global. This was later updated in 2022 to include 44,929 mining sites across 117 countries, covering 101,583 km^2 (Maus et al., 2022). Complementing this effort, Liang et al. (2021) produced a global-scale geospatial dataset of mine areas, comprised of 24,605 mine area polygons that add up to 31,396.3 km^2 globally, of which 45.6 % (11,221 polygons) were cross-validated against the dataset of Maus et al. (2020). This validation revealed high spatial consistency, with misclassification rates below 1 % in overlapping regions. Most recently, Tang and Werner (2023) produced a finely delineated global mining footprint from high-resolution satellite imagery, mapping 74,548 polygons over ~66,000 km^2 of features such as waste rock dumps, pits, water ponds, tailings dams, heap leach pads, and processing/milling infrastructure. It finds a smaller area than Maus et al. (2022), but is more finely delineated. While visually interpreting satellite imagery is a precise and effective method, it remains costly and time-consuming. Importantly, uncertainties in mine area delineation persist, primarily stemming from subjectivity in visual interpretation, temporal limitations in satellite image availability, and variations in sensor geometric precision. Beyond mapping efforts, automated methods are increasingly being developed that take these mining polygons as analytical entry points. For example, Li et al. (2025) employed machine learning with Earth observation data to construct a high-resolution global copper mining database, mapping 1,313 sites (~7,267 km^2) with detailed land use categories such as pits, waste rock dumps, and tailings facilities. This work highlights the potential of automated methods to improve consistency and efficiency in mining footprint monitoring.

Monitoring land surface disturbances in mining areas through time series analysis based on delineated mining boundaries provides an effective approach for capturing long-term changes associated with surface mining. Among various remote sensing indicators, vegetation indices such as NDVI and the Enhanced Vegetation Index (EVI) have been widely used to detect and quantify vegetation loss and recovery in mining landscapes (Jacquin et al., 2010; Karan et al., 2016). These indices are sensitive to variations in vegetation cover and condition, making them suitable for tracking disturbance and reclamation processes using satellite imagery over extended temporal scales. For example, He et al. (2023) coupled the Land Surface Temperature (LST) and NDVI to monitor surface mining disturbances using Landsat time series. The study focused on surface mining disturbances of the Huolinhe Coalfield, one of the largest mines in China. Commonly used algorithms for time-series change detection in land surface monitoring include Landsat-based detection of Trends in Disturbance and Recovery (LandTrendr) (Kennedy et al., 2010) and the Continuous Change Detection and Classification (CCDC) method (Jiang et al., 2022a). These methods are designed to identify temporal breakpoints or gradual trends in surface reflectance or vegetation indices, enabling the detection of disturbance and recovery processes over long periods and have been applied in various studies on mining-induced land surface dynamics. For example, Xiao et al. (2020b) mapped annual land disturbance and reclamation in a surface coal mining region using Google Earth Engine and the LandTrendr algorithm. While LandTrendr and CCDC perform well for monitoring land cover within individual or local mining

https://doi.org/10.5194/essd-2025-583
Preprint. Discussion started: 12 November 2025

areas, global-scale studies on land cover in mining areas remain insufficient (Jiang et al., 2022b; McKenna et al., 2020; Mi et al., 2019; Yang et al., 2018). At the worldwide scale, Yu et al. (2018) produced a mining dataset that includes land cover change information for mining areas by analyzing multi-source datasets, including NTL, MODIS, Landsat and high-resolution images from Google Earth. However, it was last updated in 2013 and is based on traditional MODIS datasets, which cover only a limited portion of global surface mining activities due to a lack of high spatial and temporal resolution datasets.

Despite the great effort to map mines globally, existing datasets lack temporal information, providing limited ability to determine the activity status in each mining patch, such as whether open-pit mining areas are in active extraction or re-greening phases through reclamation. This study presents a systematic approach to fuse mining datasets, incorporating land change detection and morphological optimization to merge and refine surface mining patch boundaries to derive temporal indicators of activity. We further extracted temporal information on land degradation and reclamation within mining areas from 1985 to 2022 and employed a decision-tree algorithm to classify the activity status of mining polygons. The dataset was validated using random stratified sampling, achieving an overall accuracy of 67 %. Compared to existing datasets, it demonstrates improved accuracy in both the number of mining sites and boundary delineation, while filling the gap in temporal information on land disturbance within mining areas. This study provides a robust dataset for sustainable mining management and ecological monitoring, enabling a better understanding of the spatiotemporal dynamics of mining-induced environmental impacts.

2 Materials and methods

This study adopts an integrated strategy that combines multiple mining datasets with land change detection and morphological optimization to harmonize and refine surface mining boundaries, thereby deriving temporal indicators of mining activity. Temporal dynamics of land degradation and reclamation from 1985 to 2022 were further extracted, and a decision-tree algorithm was applied to determine the activity status of each mining patch. Figure. 1 presents a detailed chart illustrating the workflow of this study. Four major steps can be distinguished: (1) Refinement of mining area boundaries; (2) Monitoring of temporal and spatial processes of disturbance in the mining area; (3) Classification of disturbance types in the mining area; (4) Validation.

https://doi.org/10.5194/essd-2025-583
Preprint. Discussion started: 12 November 2025

Open Access Earth System Science Data Discussions

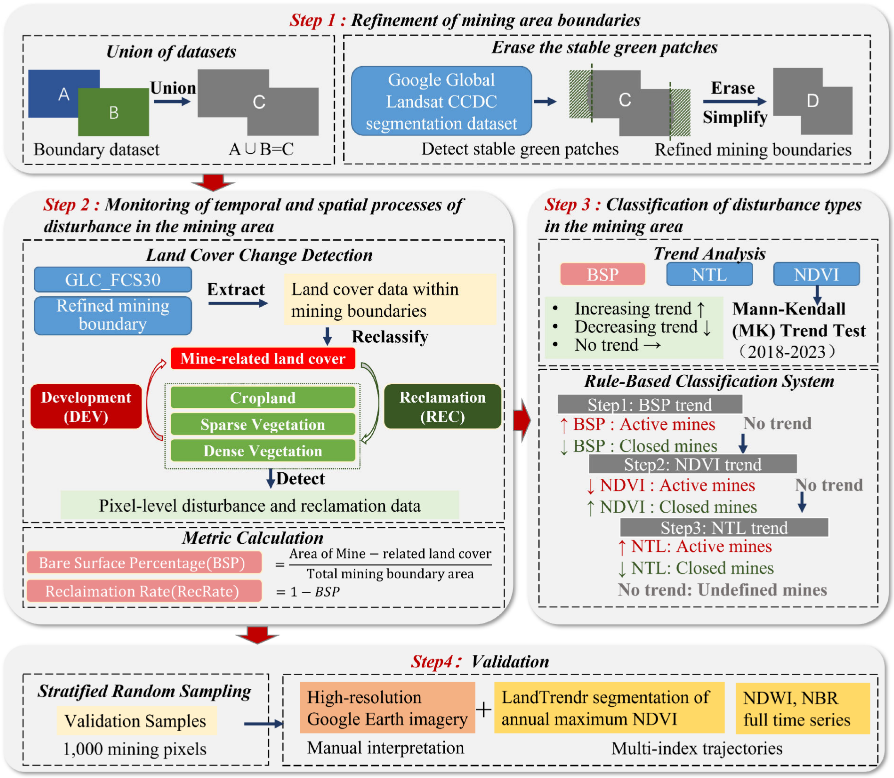

Figure. 1 The four steps of the study workflow.

2.1 Refinment of mining area boundaries

To enhance the accuracy of surface mining area boundaries, a multi-step preprocessing workflow was applied to refine the original global mining boundary dataset, encompassing data integration, classification reconstruction, stable green area exclusion, boundary overlap identification, and geometric simplification.

Step 1: Dataset integration and removal of duplicate/intersecting areas. Two widely used global mining boundary datasets were first integrated: Dataset A (74,548 polygons, 65,585 km^2) from Tang and Werner (2023) and Dataset B (44,929 polygons, 101,583 km^2) from Maus et al. (2022). Through merging and union operations, a new Dataset C was generated, comprising 82,078 polygons covering 120,043 km^2.

Step 2: Identification of stable green areas. To delineate truly disturbed regions within mining boundaries, we combined the Google Global Landsat-based CCDC Segments (1999-2019) (Gorelick et al., 2023) with a current-epoch land-cover map from the global 30-meter land cover time-series dynamic remote sensing dataset (GLC_FCS30D) (Zhang et al., 2024) to extract areas with stable vegetation cover. This combination leverages long-term, consistent, and high-resolution observations to reliably extract areas of stable vegetation cover and detect mining-related vegetation changes. Pixels

https://doi.org/10.5194/essd-2025-583
Preprint. Discussion started: 12 November 2025

were labeled as stable green if they (i) exhibited no CCDC-detected temporal breakpoints across 1999-2019, and (ii) were classified as vegetated in the current land-cover map (e.g., forest, grassland, or cropland). This yields a mask of vegetated areas that remained unchanged over the past two decades. Spatially overlapping areas with mining boundaries were assumed to be undisturbed or ecologically restored and thus erased from the boundaries.

Step 3: Edge-area erasure strategy. Stable green pixels were aggregated into polygon objects, and erasure was performed at the object level. Only stable green polygons that intersected mining boundaries were erased to avoid misclassifying native or residual vegetation located along pit margins and haul-road edges as mining disturbance. Stable green polygons entirely enclosed within mining boundaries (i.e., not intersecting the boundary) were retained, as they likely represent enclosed features predating mining or non-mining inclusions rather than genuine reclamation or undisturbed zones. By erasing only boundary-intersecting polygons that showed no change during 1999-2019, we obtained the maximum potential mining disturbance boundary—the cumulative outer envelope of mining-induced land disturbance over the study period.

Step 4: Boundary jaggedness simplification and smoothing. Erasure of green polygons introduced jagged irregularities in boundary segments. A distance-thresholding method was applied for smoothing: adjacent boundary points within 100 meters and approximately collinear were simplified into straight line segments, simplifying geometries. The final integrated mining boundary dataset contains 74,726 polygons with a total area of 82,552 km^2.

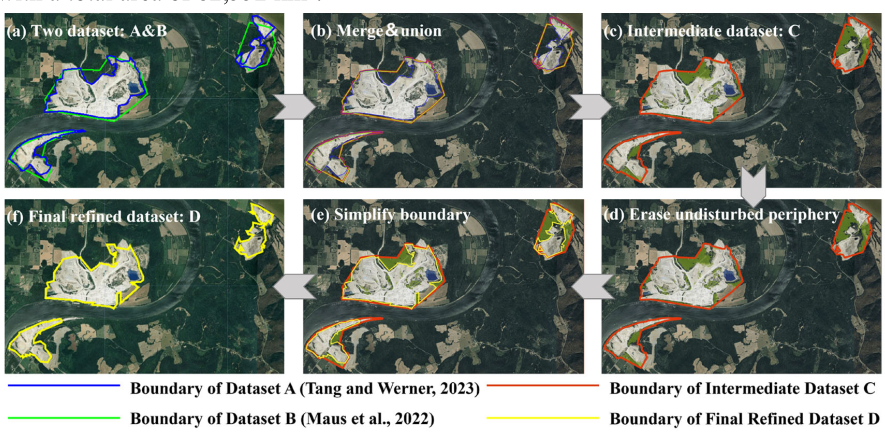

Figure. 2 Workflow of Refinment of mining area boundaries (Example Mining Area: 38.1353° N, 86.3544° W). (a) Two input datasets: Dataset A (blue lines; 74,548 polygons, 65,530 km^2) (Tang and Werner, 2023) and Dataset B (green lines; 44,929 polygons, 101,583 km^2) (Maus et al., 2022). (b) Merging and union of the two input datasets. (c) Intermediate Dataset C (red lines; 82,078 polygons, 120,043 km^2); (d) Erasure of undisturbed peripheral areas. (e) Boundary simplification. (f) Final Refined Dataset D (yellow lines; 74,726 polygons, 82,552 km^2).

https://doi.org/10.5194/essd-2025-583
Preprint. Discussion started: 12 November 2025

2.2 Monitoring the spatiotemporal dynamics of mining-induced disturbance

We analyzed land use changes within mining boundaries from 1985 to 2022 using the GLC_FCS30D dataset. For consistency with the objectives of this study, the original land cover classes were reclassified into four categories: (1) Mine-related land cover, (2) Cropland, (3) Sparse vegetation, and (4) Dense vegetation. Mine-related land cover was defined to include impervious surfaces, bare areas, consolidated bare areas, unconsolidated bare areas, water bodies and flooded flats, as identified in the GLC_FCS30D dataset.

We define DEV and REC based on the following land use type changes: if a pixel transitions from Cropland, Sparse vegetation, or Dense vegetation to Mine-related land cover, it is defined as a Development area. If a pixel transitions from Mine-related land cover to Cropland, Sparse vegetation, or Dense vegetation, it is defined as a Reclamation area. Using the land use definitions outlined above and the global 30-meter land cover time-series dynamic remote sensing products (1985 - 2022), we obtained mining disturbance and reclamation data for over 74,726 surface mining polygons worldwide from 1985 to 2022, at 30 m pixel resolution. GLC_FCS30D dataset provides maps with a five-year frequency from 1985 to 2000 and annually thereafter. Thus, we performed time interpolation on the data from before 2000. We define Bare Surface Percentage (BSP) as the ratio of the area of Mine-related land cover to the total mining area boundary. Formally, it is expressed as:

$$BSP = \frac{Area\ of\ Mine - related\ landcover}{Total\ mining\ boundary\ area}$$

This formulation assumes that a reduction in bare surface extent corresponds to vegetation regrowth or land cover restoration, and thus provides a proxy for the progress of ecological reclamation within mining sites.

2.3 Classification of mining areas based on development trends

To evaluate the recent developmental trajectories (2018-2023) and current status of global surface mining areas, we employed three indicators: NDVI, BSP, and NTL. NDVI was derived from the Sentinel-2 surface reflectance dataset, which provides high-resolution multispectral observations suitable for vegetation monitoring. BSP was calculated in this study based on the GLC_FCS30D dataset. Nighttime light data were obtained from the VIIRS Day/Night Band monthly product (NOAA, dataset ID: NOAA/VIIRS/DNB/MONTHLY_V1/VCMSLCFG) via Google Earth Engine. NDVI captures vegetation restoration or degradation, BSP quantifies bare land extent, and NTL reflects human activity intensity, enabling a comprehensive assessment of mining area disturbances and reclamation. All datasets were spatially harmonized and temporally aggregated to annual time series to ensure consistency across indicators.

The Mann-Kendall (MK) trend test was employed to quantify the time-series trends of NDVI, BSP, and NTL in this study. This nonparametric statistical test is widely applied to detect monotonic trends in time-series data. The results of the analysis for each dataset are classified as follows: Increasing trend—indicating a significant positive trend ($p < 0.05$); Decreasing trend—indicating a significant negative trend ($p < 0.05$);

https://doi.org/10.5194/essd-2025-583
Preprint. Discussion started: 12 November 2025

No trend—indicating no statistically significant trend ($p \geq 0.05$). The results of the MK test are compiled into a unified DataFrame, with each mining area characterized by the trend classifications of NDVI, BSP, and NTL. Based on the combined trends of NDVI, BSP, and NTL, this study develops a rule-based decision-tree model to classify mining area disturbances.

(1) BSP trend: As an indicator of bare land exposure, BSP is prioritized in the classification hierarchy. Mining areas with a decreasing BSP trend are classified as being in a reclamation state, while those with an increasing BSP trend are classified as being in an active mining state. Mining areas with no significant BSP trend are classified in the next step based on further analysis.
(2) NDVI trend: NDVI is employed to assess vegetation restoration or degradation. Mining areas with an increasing NDVI trend are classified as being in a reclamation state, while those with a decreasing NDVI trend, reflecting vegetation loss, are classified as being in active mining. Mining areas with no significant NDVI trend are classified in the next step based on further analysis.
(3) NTL trend: NTL is utilized to assess the level of human activities. Mining areas with an increasing NTL trend are classified as being in active mining, while those with a decreasing NTL trend indicate reduced human activities or mining area closure. If no significant NTL trend is detected, the area is classified as stable or undisturbed.

Based on trend analyses of NDVI, BSP, and NTL, a rule-based decision tree model was developed to classify mining areas into three categories. The framework first determined mining status as expanding, shrinking, or stable, and subsequently mapped these into types: active mines (expanding, characterized by increasing bare land, decreasing NDVI, and/or rising nighttime light signals), closed mines (shrinking, indicated by decreasing bare land, increasing NDVI, and/or declining nighttime light signals), and undefined mines (stable, where no significant MK trend was detected in NDVI, BSP, or NTL, or where mixed signals reflected simultaneous extraction and reclamation). By integrating the trend analyses of NDVI, BSP, and NTL, this study reveals the spatiotemporal dynamics of mining area disturbances and reclamations on a global scale.

2.4 Validation

We conducted stratified random sampling over 25 years (1990, 1995, and 2000-2022) to assess the temporal accuracy of the proposed method in detecting mining-reclamation transition years. For each year within the sampling period, 40 mining-related pixels were randomly selected using a stratified sampling strategy, resulting in a total of 1,000 validation samples. Figure. A1 shows the spatial distribution of all validation samples. Reference labels were generated through visual interpretation of high-resolution Google Earth imagery. To enhance the consistency and accuracy of interpretation, LandTrendr-derived segmentation of the annual maximum NDVI time series was integrated, along with complementary spectral profiles from Normalized Difference Water Index (NDWI) and Normalized Burn Ratio (NBR) indices. All three

https://doi.org/10.5194/essd-2025-583
Preprint. Discussion started: 12 November 2025

indices (NDVI, NDWI, and NBR) were derived from Sentinel-2 MSI surface reflectance data.

The spatial location of the sample and the accuracy verification results using NDVI, NBR, NDWI, and high-resolution Google Earth imagery are presented in Fig. 3. Figure. 3a illustrates the location of the sample mine on the island of Borneo in Indonesia. Figure. 3b shows spectral validation results for a selected sample point. The upper graph illustrates the NDVI time series (blue), LandTrendr segmentation results (orange), and the mining year inferred from the land cover time series (LCTS) as a red vertical dashed line. The lower graph shows the full time series for NDVI, NDWI, and NBR, with each point representing a satellite observation. These indices respectively reflect vegetation greenness, surface water presence, and vegetation structural change. The spectral trajectories indicate a stable condition before 2015, followed by clear disturbance signals in 2015. The mining year inferred from the LCTS, however, is 2018, highlighting the potential temporal discrepancy between spectral evidence and land cover-based detection.

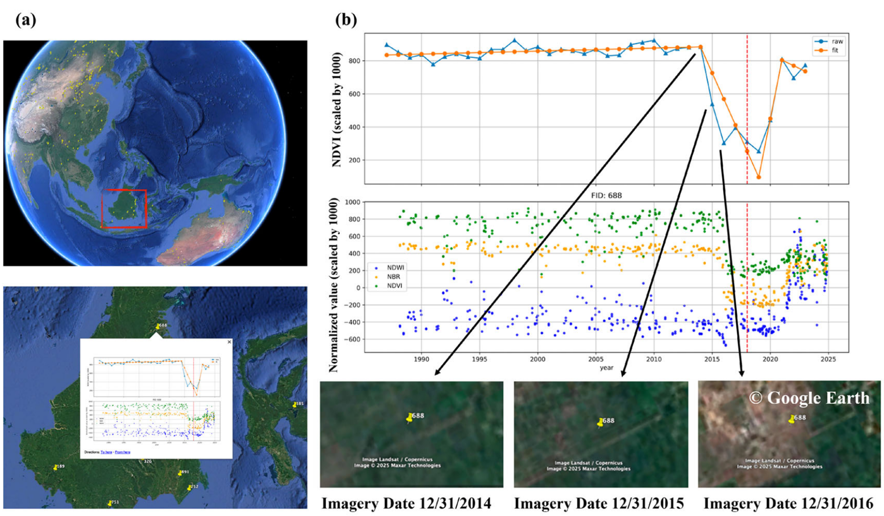

Figure. 3 (a) Spatial location of a sample mine Spatial location of a sample mine (WGS84: 3.54386°N, 117.18742°E) located on the island of Borneo, Indonesia; (b) Accuracy verification results using NDVI, NBR, NDWI, and high-resolution Landsat imagery (accessed via Google Earth).

3 Results

3.1 Spatial distribution characteristics of global mine areas

Global surface mining exhibits pronounced spatial heterogeneity in both scale and intensity. At the continental and national levels, mining activities are unevenly distributed, with certain regions concentrating a disproportionately large number of sites or total area. Distinct spatial patterns also emerge, reflecting divergent development models—ranging from fragmented small-scale operations in Asia to

https://doi.org/10.5194/essd-2025-583
Preprint. Discussion started: 12 November 2025

centralized large-scale mines in countries such as Australia and Brazil. Beyond these spatial trends, a critical ecological concern arises from the overlap between mining areas and Key Biodiversity Areas (KBAs), where intensive extraction activities directly threaten globally significant ecosystems and species (Boldy et al., 2021; Li et al., 2020; Lv et al., 2019; Sonter et al., 2018; Tai et al., 2020).

This study identifies 74,726 surface mine area polygons globally, encompassing a cumulative areal extent of 82,552 km^2, with an arithmetic mean of 1.10 km^2. Figure. 4a illustrates the global distribution of mining polygons, together with their area and count aggregated along latitude and longitude. Figure. A2 shows the global mining density in a 100 km grid. The analysis was performed in an equal-area projection (Interrupted Goode Homolosine), while the visualization uses the PlateCarree projection. Mining area densities range from 0 to 15.13 % per fishnet, at an average of 0.19 %.

Asia hosts the largest share in both number and areal extent, with 37,304 polygons (49.9 %) spanning 26,992 km^2 (32.7 %), and an average site size of 0.72 km^2, indicating highly fragmented, small-scale mining (Fig. 4b). North America ranks second, comprising 11,059 polygons (14.8 %) and 14,160 km^2 (17.2 %), with a mean site size of 1.28 km^2. Europe accounts for 9,167 polygons (12.3 %) over 11,799 km^2 (14.3 %), , with a mean site size of 1.29 km^2. Africa (6,360 polygons, 8.5 %; 8,801 km^2, 10.7 %) and South America (6,923 polygons, 9.3 %; 12,345 km^2, 15.4 %) exhibit comparatively larger average site sizes (1.38–1.78 km^2) due to widespread surface mining. In Oceania, dominated by Australia's mega-mines, 3,913 polygons (5.2 %) extend over 8,075 km^2 (9.8 %), with the largest mean site size globally (2.06 km^2).

The distribution of global mine areas is markedly uneven, with a strong concentration in a limited number of countries. Our dataset comprises mine area polygons from 155 countries and regions. Table A1 shows summary of per-country mine areas globally mapped in this study. The top 10 countries ranking by total mining area, including China, the United States, Australia, Russia, Indonesia, Canada, South Africa, Chile, Brazil, and Peru, comprise 70.6 % (58,268 km^2) of the global total. When extended to the top 30 countries, this proportion increases to 90.7 % (74,915 km^2), underscoring the high geographical concentration of mining activities worldwide. Table A1 presents the mining areas of the major contributing countries. China ranks first in total mining area (11,542 km^2, 14 %), driven by 27,948 mining polygons with a mean areal extent of 0.41 km^2 per site (Fig. 4c). While China has the largest number and total area of mining polygons globally, its average site size remains significantly lower than that other high mineral demand countries (e.g., India and USA) and high mineral export countries (e.g., Australia, Canada, South Africa, and Russia), where averages exceed 1 km^2. African countries, particularly in sub-Saharan Africa, show both small total areas and small scale sizes, largely due to the prevalence of artisanal and small-scale mining that occurs informally on unregulated land (Hilson et al., 2017; Oramah et al., 2015).

https://doi.org/10.5194/essd-2025-583
Preprint. Discussion started: 12 November 2025

Open Access Earth System Science Data Discussions

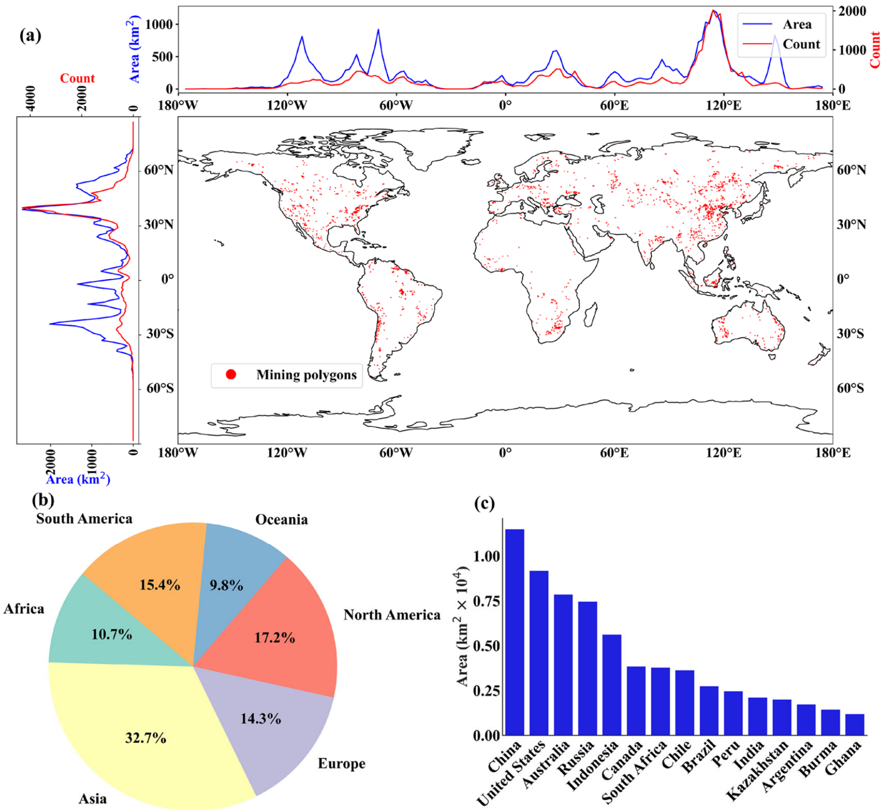

Figure. 4 Global distribution and characteristics of mining polygons. (a) Global distribution of mining polygons and their latitudinal/longitudinal statistics of area and count. Given the visualization effect, the centroids of the polygons are used for display here instead of the actual shapes of the polygons. (b) Continental proportion of the global mining polygons area. (c) Mining polygons area in the top 10 countries in terms of total mining area.

In this study, a total of 3,248 mining areas were identified within KBAs worldwide, covering a combined area of 3,986 km^2, accounting for 4.8 % of the global mining extent. Figure. 5a shows the global mining density within KBAs in a 100 km grid. These polygons are unevenly distributed across 105 countries and regions. Mining area densities range from 0 to 3.25 % per fishnet, at an average of 0.07 %. Table A2 shows summary of per-country mine areas within KBAs mapped in this study. Asia hosts the largest number of KBA-overlapping mining areas (1,412 polygons, 43.5 %), followed by South America (543 polygons), North America (394 polygons), and Europe (390 polygons). In terms of area, Asia also ranks highest (1,299 km^2, 32.7 %), followed by South America (1,156 km^2, 28.9 %) and Africa (512 km^2, 12.9 %) (Fig. 5b). Approximately 71 % of the polygons are situated within 10 countries: China, Brazil, Argentina, Mexico, Australia, South Africa, Indonesia, Namibia, Burma, and Venezuela

https://doi.org/10.5194/essd-2025-583
Preprint. Discussion started: 12 November 2025

(Fig. 5c). China alone accounts for 858 mining areas (26.3 %) within KBAs, with a total area of 682 km^2 (17.1 %). Brazil (244 polygons, 443 km^2) and Argentina (22 polygons, 427 km^2) also show considerable overlaps area despite fewer polygons. Notably, Argentina shows largest average area per polygon (19 km^2), indicating the presence of large-scale operations within sensitive ecological regions. In contrast, countries such as Australia and Mexico exhibit moderate overlap both in terms of site count and area. These results highlight spatial clustering of mining pressure within biodiversity-priority regions, particularly in Asia and South America. The coexistence of high biodiversity value and intensive mining underscores the urgent need for spatially targeted conservation strategies and the integration of ecological sensitivity into mining governance frameworks.

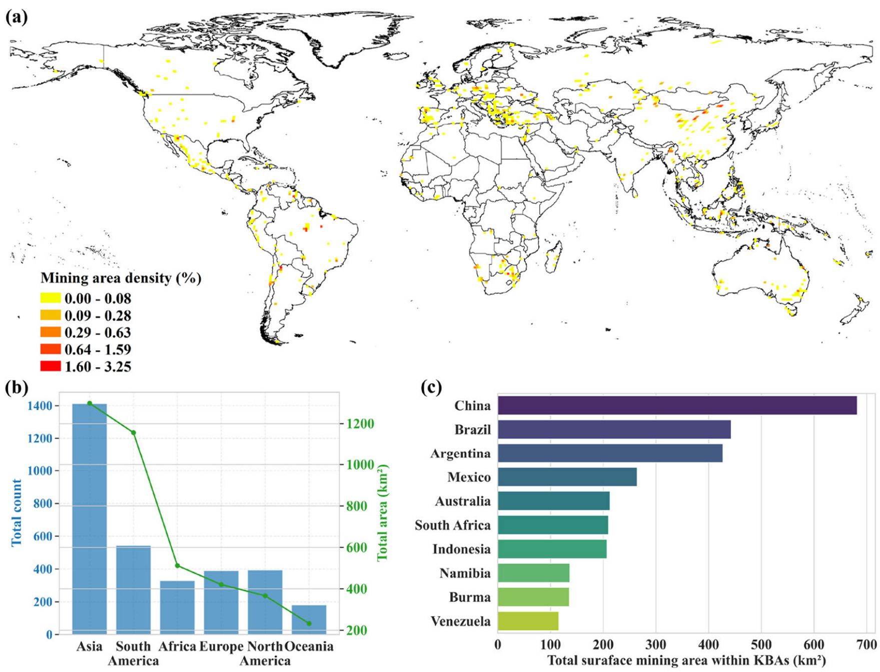

Figure. 5 Global distribution and characteristics of mining polygons within KBAs. (a) Global mining density within KBAs in a 100 km grid. Mining area density is calculated as the proportion of mining area within 100 x 100 km (10,000 km^2) grid cells. Data was aggregated using the Interrupted Goode Homolosine equal-area projection to ensure accurate area calculations. The map is displayed using the PlateCarree projection. The boundary and attribute data of KBAs used in this study are obtained from the World Database of Key Biodiversity Areas (https://www.keybiodiversityareas.org/). (b) Counts and total area of mine within KBAs by world regions. (c) Top 10 countries by mining area within KBAs.

3.2 Monitoring of spatiotemporal process of disturbance in mining area

Mining activities lead to substantial modifications in land cover. By tracking land cover change at the pixel level within delineated mining boundaries, we analyzed the global spatiotemporal dynamics of land disturbance and reclamation from 1985 to 2022. Over this period, the cumulative area of land disturbed by surface mining reached 40,596 km^2, accounting for approximately 49 % of the total global surface mining footprint. In comparison, the reclaimed area totalled 29,285 km^2. The annual land disturbance and reclamation areas showed distinct temporal dynamics during 1985–2022, with phase shifts in both magnitude and relative balance (Fig. 6a).

From 1985 to 2000, for the mine areas included in the study, the annual disturbed area surged from 214 km^2 to 940 km^2, while the annual reclamation area expanded more slowly from 82 km^2 to 357 km^2, resulting in a substantial gap indicative of delayed ecological restoration. During 2001–2010, both metrics continued rising to 1541 km^2 (disturbance) and 1030 km^2 (reclamation) with decelerated rates (36.7 km^2 vs. 18.4 km^2 yr^{-1}), and the positive gap narrowed gradually. From 2011 onward, the disturbed area exhibited pronounced fluctuations, peaking at 1,943 km^2 in 2015, followed by a steady decline to 1,373 km^2 in 2022. In contrast, the reclaimed area continued to rise with interannual variability and reached a maximum of 1,735 km^2 in 2021. A notable transition occurred in 2018, when the reclaimed area (1,576 km^2) first exceeded the annual disturbed area (1,569 km^2), marking a shift toward net ecological recovery. This turning point underscores a global shift toward intensified ecological restoration. For example, in China, ecological rehabilitation of mining areas has long been prioritized, with national programs over the past four decades focusing on vegetation recovery and the mitigation of geological hazards. Furthermore, the Chinese government has ordered the closure of over 20,000 mines, and these sustained efforts have led to significant advances in mine land reclamation (Chen et al., 2025a; Xiao et al., 2020c). Quantification of the disturbance-reclamation gap (i.e., disturbance area minus reclamation area) confirms consistent positive values (net degradation) during 1990–2017, shifting to negative values post-2018, indicating a global transition to net land recovery.

We analyzed land disturbance and reclamation in global surface mining areas across five landcover types: cropland, forest, grassland, shrubland, and sparse vegetation from 1985 to 2022. Cropland had the largest damaged area (13,623 km^2, 34 %), followed by shrubland (8,464 km^2, 21 %), grassland (7,836 km^2, 19 %), sparse vegetation (5,262 km^2, 13 %), and forest (5,411 km^2, 13 %) (Fig. 6b). For land reclamation, cropland also boasted the largest cumulative reclaimed area (9,082 km^2, 31 %), with shrubland (6,716 km^2, 23 %), grassland (5,885 km^2, 20 %), sparse vegetation (4,221 km^2, 14 %), and forest (3,380 km^2, 12 %) following in sequence. Despite ongoing reclamation efforts, considerable differences remain between disturbed and restored land cover types. Here, “reclamation” refers to areas showing vegetation recovery, which may result from both active restoration practices and natural regrowth in abandoned polygons. We calculated the gap between damaged and reclaimed areas for annual areas of each landcover type (Fig. A3 and Fig. 6c). As of 2022, approximately 4,541 km^2 of cropland (33.3 %) and 2,039 km^2 of forest (38 %) were disturbed by unreclaimed mining areas. In contrast,

https://doi.org/10.5194/essd-2025-583
Preprint. Discussion started: 12 November 2025

the unreclaimed proportions for grassland, shrubland, and sparse vegetation are relatively lower, at 25 %, 21 %, and 20 %, respectively. This discrepancy may reflect differences in post-mining land use suitability, ecological fragility, or restoration policies targeting specific land cover types.

Notably, although the forest had the lowest damaged area among all land types, the gap between its disturbance and reclamation showed a relatively compact and continuously positive distribution. The box plot revealed that the net gap in most years was concentrated in the 0–100 km^2 range, with almost no extreme outliers, reflecting the overall low disturbance intensity of forest ecosystems. However, unlike other landcover types where reclaimed area exceeded damaged area in some years, the forest was almost in a "net damage" state throughout the year. This persistent reclamation lag may stem from the long natural recovery period of forests or insufficient current restoration measures for forest ecosystems (Poorter et al., 2021). Moreover, considering the crucial role of forests in biodiversity protection and carbon storage, even a small absolute damaged area can have significant ecological consequences per unit of disturbance (Cook-Patton et al., 2020; Feng et al., 2022).

Among all mining-induced land disturbances globally, Asia contributed the largest share, particularly in cropland and grassland areas. Approximately 6,414 km^2 of disturbed cropland (47 % of the global total) and 4,532 km^2 of disturbed grassland (58 %) were located in Asia (Fig. A4). Within the region, China ranked first in both disturbed and reclaimed land areas, accounting for about 22 % of global cropland loss and 40 % of global grassland loss (Fig. 6d). Besides, forest disturbances were primarily observed in Russia, Canada, and Indonesia, contributing 20 %, 13 %, and 11 % of the global total, respectively. Shrubland loss was concentrated in North America (25 %) and Africa (23 %), with the United States alone contributing 16.5 %.

By 2023, the global average reclamation rate of surface mining land reached 70.3 %, indicating substantial progress in land restoration efforts worldwide. Nevertheless, pronounced regional disparities remain. Oceania and Africa exhibited the highest reclamation rates, whereas Asia and Europe were approximately 10 % lower than the global average. Figure. 4e illustrates the spatial distribution of reclamation by showing the percentage of bare surface area within mining regions at a 100-km resolution in 2022. The reclamation rate is calculated as 1-BSP and represents the proportion of vegetated land within mining areas, serving as an indicator of ecological recovery.

At the national level, countries with the largest surface mining footprints exhibited pronounced variation in reclamation performance. Figure. A5 shows the reclamation rate of top 15 Countries ranking by mining area at 2023. China, hosting the largest number of mining polygons globally, reported a reclamation rate of 59.6 %, which falls below the global average—highlighting persistent challenges in ecological restoration under high-intensity mining conditions. In contrast, other major mining countries such as the United States (73.0 %) and Australia (80.8 %) demonstrated notably higher

https://doi.org/10.5194/essd-2025-583
Preprint. Discussion started: 12 November 2025

reclamation rates, likely attributable to stronger regulatory systems and established restoration frameworks (Yonk et al., 2019). In Asia, several countries outperformed the continental average, including India (72.2 %), Kazakhstan (77.8 %), and Indonesia (76.9 %), reflecting the effective implementation of restoration practices in some contexts. In South America, while Brazil reported a high reclamation rate of 81.2 %, followed by Peru (63.0 %), countries such as Chile (53.3 %) exhibited considerably slower progress, indicating persistent internal disparities across the region. In Africa, resource-dependent economies such as Ghana (83.7 %) and the Democratic Republic of the Congo (79.6 %) also showed encouraging reclamation trends. The major mining countries of Russia (62.4 %) and Ukraine (71.4 %) reported moderate reclamation rates.

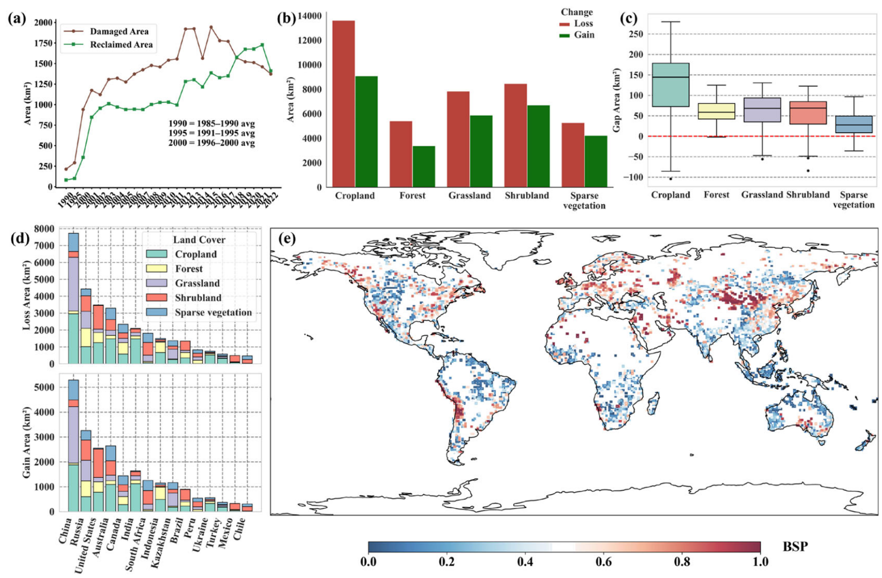

Figure. 6 (a) Annual land disturbance and reclamation area of global surface mines (1985-2022). To ensure the continuity of the graph, the values for 1990, 1995, and 2000 correspond to the average annual changes over five-year intervals—specifically, they represent the five-year averages for the periods 1985–1990, 1991–1995, and 1996–2000, respectively. (b) Gain and loss of land cover types during mining disturbance events. (c) Boxplot of "gap" for land cover types (gap = loss - gain). (d) Losses and gains of five land cover types in the top 15 countries ranked by total area of land with changes. (e) Percentage of bare surface area in global mining areas, aggregated to 100 km resolution (2022).

3.3 Classification of global surface mining areas

Overall, the global distribution of mining development status reveals a dominant trend of active mining, both in terms of site counts and spatial extent, with notable regional and national variations. Figure. 7a presents the classification of the development status of mining areas over the recent years, encompassing three categories: active, undefined, and closed. For the change maps corresponding to each development status category,

https://doi.org/10.5194/essd-2025-583
Preprint. Discussion started: 12 November 2025

Open Access Earth System Science Data Discussions

two distinct change directions are denoted by specific colors: Red pixels indicate a land cover transition from non-mining-related types to mining-related types, representing the expansion of mining areas. Green pixels indicate the inverse transition—from mining-related land cover types to non-mining-related types—representing the shrinkage of mining areas.

Globally, of the 74,726 surface mining polygons identified, 14,546 (19.5 %) were classified as closed mines, 36,542 (48.9 %) as undefined mines, and 23,638 (31.6 %) as active mines (Fig. 7b). In terms of area, active mines accounted for 30,147 km^2 (36.5 % of the global total), followed by closed mines at 25,389 km^2 (30.8 %). These results indicate that active mining areas dominate both numerically and in spatial extent worldwide. Regional analysis (Fig. 7c) shows that active mines outnumber closed mines across all continents except Europe, which is the only continent having more closed mines (2003) than active mines (1885). Mineral-rich Africa exhibits the lowest proportion of closed mines (18.7 %) and the highest proportion of active mines (33.5 %) (Ross and Werker, 2024). Asia has approximately 20.0 % of green mines and 32.0 % active mines, with 11,953 active mines representing 50.6 % of the global active mine count, highlighting intensive mining operations. In North America, active mines constitute 33.5 % of polygons, underscoring their role as major mineral producers (Giljum et al., 2025).

Among the major mining countries, almost all exhibit a predominance of active mines over closed mines, indicating that most nations remain in an expansionary phase of mining development (Fig. 7d). Fourteen of the fifteen leading mining countries follow this pattern, with South Africa as the sole exception. Several major mining nations, including China, the United States, Australia, Russia, Indonesia, and Canada, show a markedly higher proportion of active mines relative to closed mines. China, which possesses the largest mining area globally, and the United States, ranking second, both display similar proportions, with active mines accounting for approximately 31 % and closed mines around 21 %. Chile has the highest share of active mines (52.0 %) and one of the lowest shares of closed mines (12.4 %), reflecting its copper-dominated sector's strong reliance on ongoing mineral extraction (Abbas et al., 2024). Peru shows a similar trend, with closed mines comprising only 10.4 % and active mines 33.8 %. In contrast, South Africa stands out as the only major mining country where closed mines (30.1 %) exceed active mines (19.4 %), diverging from the overall global trend.

https://doi.org/10.5194/essd-2025-583
Preprint. Discussion started: 12 November 2025

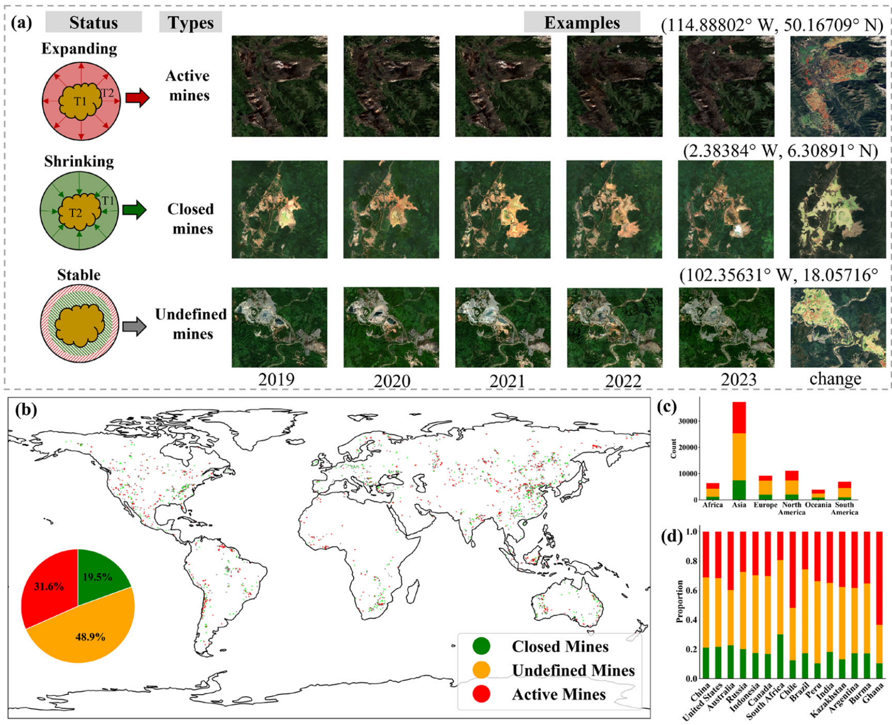

Figure. 7 (a) Classification of development status of mining areas in the recent five years: active, undefined, closed. While the figure illustrates the period 2019–2023, the actual dataset used spans from 2018 to 2023. (b) Global distribution of three types of mining areas. (c) Continental counts of mining areas types (d). Type structures of the top 15 countries (sorted by total mining areas descendingly).

4 Discussion

4.1 Comparison of results of prior mining area datasets

Our refined global surface mining area dataset demonstrates substantial improvements in comprehensiveness, offering detailed insights into spatiotemporal processes related to mining and reclamation. Compared with existing datasets, it achieves greater completeness in terms of data volume, while also filling the gap in long-term spatiotemporal change information of mining - induced land disturbances.

To evaluate its performance, we systematically compared our dataset against two widely used global mining boundary datasets—Dataset A (Tang and Werner, 2023) and Dataset B (Maus et al., 2022)—as well as the intermediate merged dataset (Dataset C) generated during our workflow (Fig. 2). Dataset A comprises 74,548 polygons (65,585 km^2) and delineates mining areas with relatively tight outlines, thereby capturing polygon shape variability in detail. In contrast, Dataset B consisting of 44,929 polygons (101,583 km^2), applies a 10 km manual buffering approach that broadly encompasses mining extents but frequently exaggerates disturbed areas. These

https://doi.org/10.5194/essd-2025-583
Preprint. Discussion started: 12 November 2025

methodological differences are evident in Fig. 2a, where the boundaries from Maus et al. (2022) (green lines in Fig. 2a) cover much larger regions, whereas the boundaries from Tang and Werner (2023) (blue lines in Fig. 2a) are more closely aligned with actual mine features. Building on these, the boundaries of our refined dataset (yellow lines in Fig. 2f) further improve delineation by more accurately fitting the true extent of mining disturbances, thereby reducing both overestimation and omission.

Our intermediate Dataset C, obtained through merging and union operations, contained 82,078 polygons (120,043 km^2), which maximized spatial coverage but introduced redundancy and misclassification. Through multi-step optimization, we refined this dataset to 74,726 polygons (82,552 km^2), thereby striking a balance between coverage and accuracy. Compared with Maus et al. (2022), our dataset contains 165 % of its polygons while covering only 81.3 % of its total area, effectively reducing boundary overestimation. Relative to Tang and Werner (2023), our dataset adds 178 polygons and represents 125.9 % of its mapped area. By integrating CCDC-derived land surface dynamics with fine-resolution land cover datasets, we erased long-term stable vegetation patches and eliminated spurious inclusions, which led to a 31.2 % reduction (37,493 km^2) in overestimated areas compared with the simple merged result. This refinement yields the maximum potential mining disturbance boundary, defined as the cumulative outer envelope of mining-induced land disturbance across the study period, thereby substantially improving boundary precision. As summarized in Table 1, the refined dataset (present study) balances spatial coverage and accuracy, reducing both overestimation and omission, and thus provides a more reliable basis for global-scale mining disturbance assessments.

In this study, we analyzed the spatiotemporal dynamics of 74,726 mining polygons worldwide, covering the period from 1985 to 2022, and further examined recent development trends of mining areas. The monitoring of mining disturbance and reclamation processes was conducted at the pixel scale, enabling fine-grained tracking of temporal land-use transitions within each mining site. By comparison, Yu et al. (2018) focused on the spatial locations of 790 mines and carried out time-series monitoring of land-cover changes, but its temporal coverage was limited to the 1980s–2013. Our dataset not only extends the temporal span to nearly four decades (1985–2022) but also substantially broadens the scope to a global coverage of 74,726 mining polygons. In addition, we classified the current development status of mines into three categories—active, closed, and undefined—providing a new dimension of information that complements previous datasets. The broader spatial coverage, combined with improved temporal resolution and accuracy, offers enhanced capacity to track fluctuations in both mining expansion and reclamation. This advancement facilitates a more comprehensive understanding of the temporal evolution of global surface mining disturbances and establishes a stronger foundation for ecological restoration research and impact assessment in mining regions.

Table 1 Comparison of results with prior mine area studies.

https://doi.org/10.5194/essd-2025-583
Preprint. Discussion started: 12 November 2025

Source	Regions /scales	Mines /Polygons	Occupied land (km^2)	Average area (km^2)
(Tang and Werner, 2023)	Global	74,548	65,585	0.88
(Maus et al., 2022)	Global	44,929	101,583	1.8
(Liang et al., 2021)	Global	24,605	31,396	1.3
(Maus et al., 2020)	Global	21,060	57,277	2.7
Present Study	Global	74,726	82,552	1.1

4.2 Advantages of this method and future application directions

By integrating and refining existing datasets and applying automated morphological optimization, this study substantially improved both the coverage and boundary accuracy of global surface mining area delineation relative to previous products. Specifically, the delineated boundaries were enhanced by erasing stable green pixels—identified through the Google Global Landsat-based CCDC Segments (1999–2019) and the GLC_FCS30D dataset—that intersected with mining polygons over a 20-year period. This procedure effectively reduced misclassification of non-mining vegetation within mining extents, thereby increasing the spatial precision of boundary mapping. As a result, we derived the maximum potential mining disturbance boundary, defined as the cumulative outer envelope of mining-induced land disturbance throughout the study period. This approach not only ensures more reliable detection of historical mining footprints but also provides a solid data foundation for future monitoring of disturbance–reclamation dynamics at multiple spatial and temporal scales.

For classifying development trends of mining areas, we integrated three remote sensing-derived indices, NDVI, BSP, and NTL, that capture spatiotemporal changes from multiple dimensions. NDVI, BSP, and NTL represent vegetation recovery, bare soil exposure, and human activities, respectively, providing a robust framework for disturbance analysis. The non-parametric MK test effectively reduces noise and irregular fluctuations in the data, ensuring the reliability and stability of trend analysis. This approach objectively and accurately detects monotonic trends in diverse datasets, providing a solid scientific basis for classifying disturbance types. Moreover, the method is simple, transparent, and easy to implement, making it suitable for large-scale spatial data analysis. Classification rules and data processing methods can be adjusted according to the specific characteristics of different mining areas.

Future research can integrate more detailed ecological restoration monitoring data, ecological environment data, human activity data, and socioeconomic data by incorporating the spatial boundaries of mining areas and time-series data on internal land disturbances. This integration will enable exploration of the impacts and relationships between global surface mining and the ecological environment, as well as help human society better distinguish different qualities of restored ecosystems after reclamation of former mining areas.

https://doi.org/10.5194/essd-2025-583
Preprint. Discussion started: 12 November 2025

4.3 Uncertainty and limitations

This study is subject to several uncertainties and limitations stemming from the input data and the methodological framework. First, the temporal baseline of the analysis is constrained by the GLC_FCS30D dataset, which commences in 1985. Consequently, mining disturbances and any subsequent reclamation activities occurring prior to this date are not captured in our results. Furthermore, the temporal granularity of this dataset is coarse prior to 2000, with observations limited to five-year intervals. This reduces the precision for pinpointing the exact timing of disturbance and reclamation events, particularly in the early decades of the study period. Uncertainty is also introduced through the classification schemes inherent in global land cover products. For example, cropland appears as the largest cumulative reclaimed area, likely reflecting misclassification of early successional vegetation, bare soil, or agricultural areas rather than actual land use (Sonter et al., 2025).

A primary methodological limitation is the sensitivity of the disturbance detection algorithm. The approach identified disturbance signals across 40,596 km^2, corresponding to approximately 49 % of the total delineated mining area. The remaining 51 % of the area did not exhibit a detectable disturbance signature under our framework. This incomplete detection rate can be attributed to a combination of inherent uncertainties within the GLC_FCS30D source dataset and the intrinsic limitations of the algorithm in capturing the complex spectral-temporal signatures of highly dynamic mining environments. Furthermore, the reliability of vegetation-based metrics is also geographically variable, posing particular challenges in extreme environments such as arid deserts and tundra (Xu et al., 2023). In these regions, natural bare land dominates, potentially leading to high rates of false negatives, while data processing accuracy and classification reliability are generally lower, complicating the detection of mining-induced disturbances.

Furthermore, mines that lacked sufficient confidence for classification into active or closed categories were designated as "undefined." This undefined category may encompasses mines undergoing simultaneous extraction and reclamation—a scenario where concurrent increases in BSP (indicating ongoing disturbance from extraction) or NTL (indicating operational activity) and NDVI (indicating vegetation growth from reclamation) create ambiguities that hinder clear determination of their dominant status.

Finally, the reclamation rate in this study was calculated as 1−BSP, representing the proportion of vegetated cover within mining areas. While this proxy provides a consistent and scalable measure of greening by quantifying the proportion of vegetated cover within mining boundaries, it does not necessarily reflect actual reclamation practices or ecological restoration outcomes. Therefore, the global average reclamation rate of 70.3 % reported for 2023 should be viewed as an indicator of vegetation presence, which likely overestimates the extent of true ecological recovery.

The accuracy assessment covered 14 major terrestrial ecoregion types globally,

https://doi.org/10.5194/essd-2025-583
Preprint. Discussion started: 12 November 2025

commonly referred to as "biomes", such as Boreal Forests/Taiga, Deserts and Xeric Shrublands, Flooded Grasslands and Savannas, and Mangroves (Olson et al., 2001). The overall accuracy was 67 %, but significant regional variations existed (Table A3). Excluding the Tropical and Subtropical Coniferous Forests (with only one sample), the 28 samples in Tropical and Subtropical Dry Broadleaf Forests showed the highest average accuracy (79 %). Four zones—Montane Grasslands and Shrublands, Temperate Broadleaf and Mixed Forests, Tropical and Subtropical Grasslands, Savannas and Shrublands, and Tropical and Subtropical Moist Broadleaf Forests—exceeded 70 % accuracy. In contrast, Deserts and Xeric Shrublands had an average accuracy of 61 %, likely due to high environmental heterogeneity and limited method adaptability in complex arid environments. The Mangroves zone exhibited a high standard deviation (0.58), indicating large fluctuations in accuracy, while Tropical and Subtropical Dry Broadleaf Forests had a lower standard deviation (0.42), reflecting more consistent results.

The confusion matrix between predicted and reference transition years (Fig. A6 a) demonstrated a clustered diagonal distribution, indicating temporal proximity between predictions and ground-truth data. Cumulative temporal accuracy analysis (Fig. A6 c) revealed 67 % of samples achieved ±5-year agreement, with progressive accuracy improvements observed at broader tolerance thresholds. Temporal lag histograms (Fig. A6 b) quantified prediction errors. Error propagation analysis identified systematic limitations: 13.7 % of samples (n=137) exhibited pre-1985 mining disturbances that were misclassified as transition events. This discrepancy arises from the land cover classification dataset's temporal scope (initiated in 1985), which prevents the detection of pre-existing disturbances. Such errors predominantly occurred in regions with legacy mining activities prior to the observational baseline.

5 Conclusion

In this study, we developed and validated a new global dataset that delineates the maximum potential disturbance boundaries for 74,726 surface mining polygons and tracks their land change dynamics from 1985 to 2022. By integrating existing products with an automated morphological optimization that systematically removed stable, non-mining vegetation, we substantially improved the spatial precision of historical mining area boundaries. The classification of mine development trends was further enhanced by integrating multi-dimensional remote sensing indices (NDVI, BSP, and NTL) within a robust Mann-Kendall trend analysis.

The resulting dataset, covering a total extent of 82,552 km², reveals the vast scale of global mining's footprint. Our analysis shows that cumulative land disturbance reached 40,596 km² (49 % of the total delineated area) over the 38-year period, while cumulative reclamation amounted to 29,285 km². Cropland was the land cover type most severely affected by surface mining. Significant disparities in reclamation progress were observed across regions, particularly in ecologically fragile areas such as the Amazon and tropical rainforests, where deforestation and delayed reclamation remain pressing

https://doi.org/10.5194/essd-2025-583
Preprint. Discussion started: 12 November 2025

issues. Over the past several years, active mines have consistently dominated, constituting 31.6 % of the total. The high share of active mines reflects the continued expansion of mining.

This high-precision boundary and disturbance dataset provides a foundational geospatial framework for the Earth system science community. Its primary value lies in addressing a critical knowledge gap by providing a new and more detailed global database that documents the long-term time series of both mining disturbance and reclamation dynamics. Ultimately, this work offers an essential data product to advance the monitoring of land degradation, assess the effectiveness of restoration efforts, and support policies aimed at achieving more sustainable mining practices globally.

Code and data availability

The global mining disturbance and reclamation dataset presented in this study is publicly available in the Zenodo repository at https://doi.org/10.5281/zenodo.17085099 (Xu et al., 2025). Code supporting this study is publicly available at GitHub: https://github.com/NickCarraway96/GlobalMiningDatabase.

Appendix A

Figure. A1 Global spatial distribution of 1,000 validation samples.

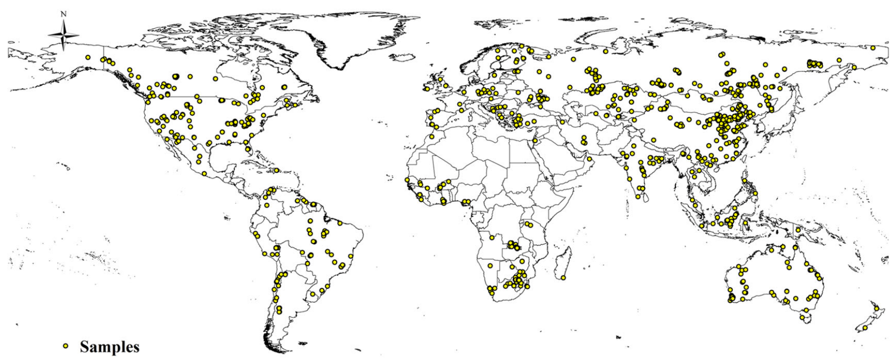

Figure. A2 Global mining density in a 100 km grid. Mining area density is calculated as the proportion of mining area within 100 x 100 km (10,000 km^2) grid cells. Data was aggregated using the Interrupted Goode Homolosine equal-area projection to ensure accurate area calculations. The map is displayed using the PlateCarree projection.

https://doi.org/10.5194/essd-2025-583
Preprint. Discussion started: 12 November 2025

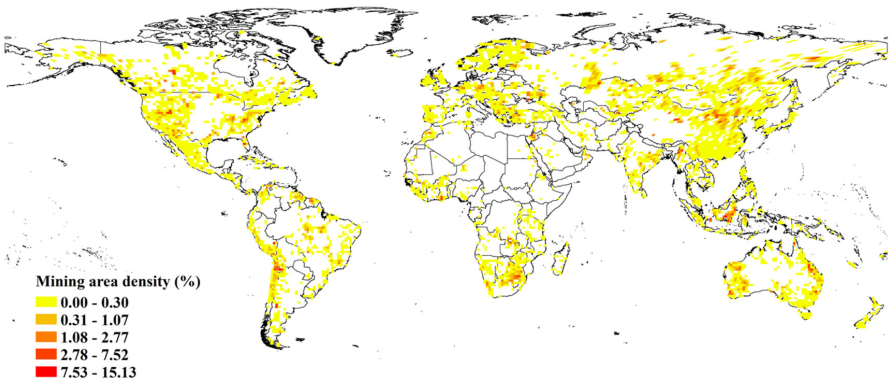

Figure. A3 Annual gap between damaged and reclaimed areas for five land cover types and total land (calculated every five years before 2000).

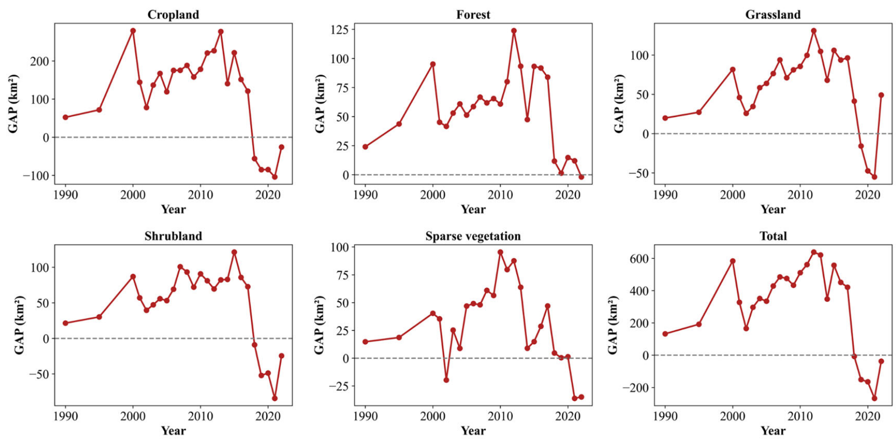

Figure. A4 Annual reclamation and damage of five land cover types across continents. To ensure the continuity of the graph, the values for 1990, 1995, and 2000 represent the average annual changes over five-year intervals.

https://doi.org/10.5194/essd-2025-583
Preprint. Discussion started: 12 November 2025

Open Access Earth System Science Data Discussions

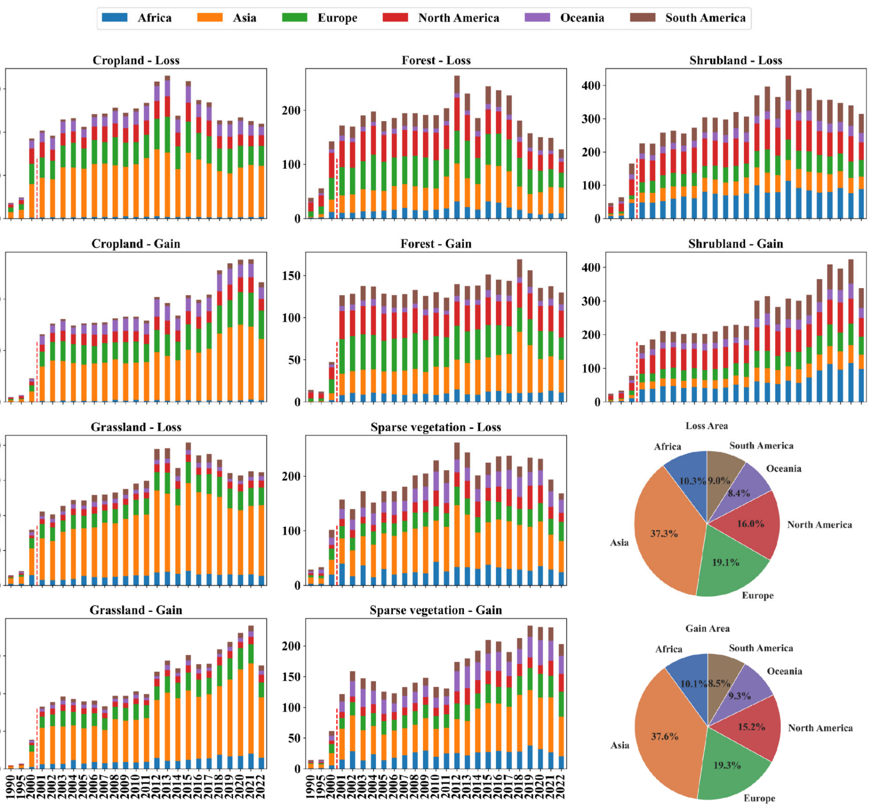

Figure. A5 Reclamation rate of top 15 countries by mining area, 2023.

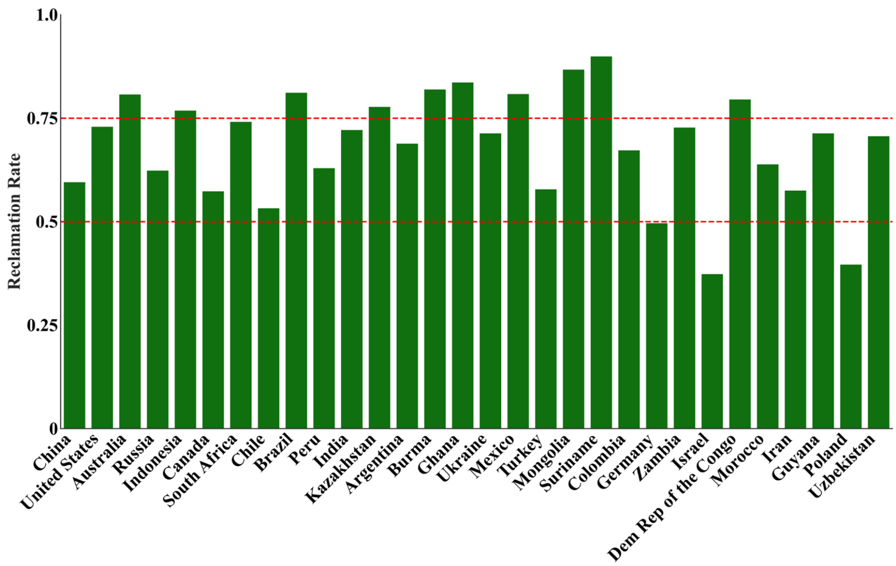

Figure. A6 Validation results. (a) Confusion matrix between predicted and reference change years; (b) Histogram of temporal lags between predicted and reference years;

https://doi.org/10.5194/essd-2025-583
Preprint. Discussion started: 12 November 2025

(c) Cumulative accuracy progression with increasing tolerance thresholds, validating the robustness of the ±5-year criterion.

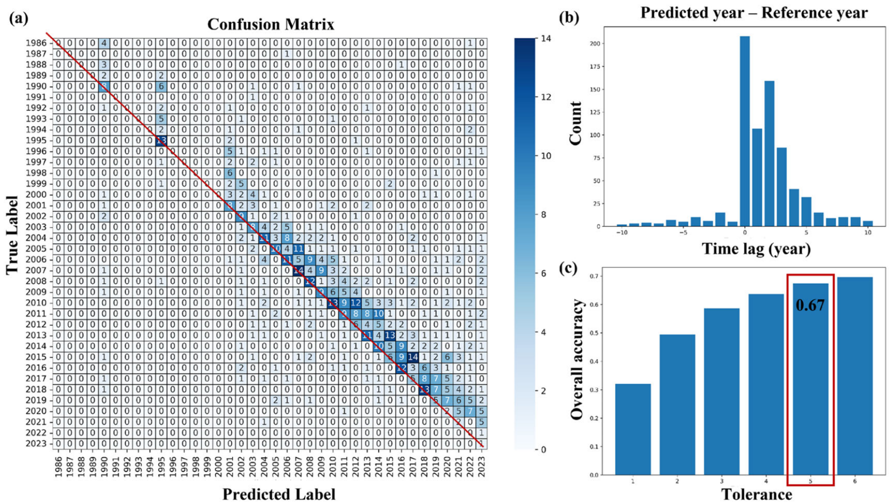

Table A1 Summary of per-country mine areas mapped in this study.

Countries	Polygons	Occupied land (km^2)	Average (km^2/polygon)
China	27948	11542.33	0.41
United States	5813	9196.03	1.58
Russia	4183	7477.71	1.79
Australia	3522	7867.07	2.23
Canada	3158	3864.09	1.22
Brazil	2753	2763.75	1.00
Indonesia	2040	5630.99	2.76
South Africa	1891	3794.82	2.01
India	1686	2124.85	1.26
Mexico	1583	820.30	0.52
Ukraine	1528	1201.34	0.79
Turkey	1117	768.48	0.69
Peru	1029	2485.79	2.42
Chile	989	3645.88	3.69
Kazakhstan	936	2014.00	2.15
Other countries (N=140)	14550	17354.57	1.19

Table A2 Summary of per-country mine areas within KBAs mapped in this study.

Countries	Polygons	Occupied land (km^2)	Average (km^2/polygon)
China	858	682.24	0.80

https://doi.org/10.5194/essd-2025-583
Preprint. Discussion started: 12 November 2025

Brazil	244	442.83	1.81
Argentina	22	427.22	19.42
Mexico	258	264.55	1.03
Australia	158	212.87	1.35
South Africa	166	209.80	1.26
Indonesia	81	207.24	2.56
Namibia	19	136.88	7.20
Burma	34	135.62	3.99
Venezuela	51	115.67	2.27
Turkey	185	99.44	0.54
Spain	64	85.96	1.34
Ukraine	15	77.93	5.20
Russia	83	67.74	0.82
United States	54	61.57	1.14
Other countries (N=90)	956	758.64	0.79

Table A3 Distribution and accuracy rate of validation samples across global biomes.

Biomes	**Sample size**	**Average accuracy rate**	**Standard deviation**
Boreal Forests/Taiga	173	0.66	0.48
Deserts and Xeric Shrublands	109	0.61	0.49
Flooded Grasslands and Savannas	5	0.60	0.55
Mangroves	3	0.67	0.58
Mediterranean Forests, Woodlands and Scrub	39	0.69	0.47
Montane Grasslands and Shrublands	53	0.72	0.45
Temperate Broadleaf and Mixed Forests	204	0.70	0.46
Temperate Conifer Forests	58	0.69	0.47
Temperate Grasslands, Savannas and Shrublands	133	0.65	0.48
Tropical and Subtropical Coniferous Forests	1	1.00	
Tropical and Subtropical Dry Broadleaf Forests	28	0.79	0.42
Tropical and Subtropical Grasslands, Savannas and Shrublands	68	0.74	0.44
Tropical and Subtropical Moist Broadleaf Forests	113	0.74	0.44
Tundra	12	0.67	0.49

https://doi.org/10.5194/essd-2025-583
Preprint. Discussion started: 12 November 2025

Earth System Science Data
Open Access Discussions

Acknowledgment

The research was supported by the National Key Research and Development Program (Approval No. 2023YFE0122300).

Author contributions

WX, SX, and JZ designed the research; SX and JZ developed the methodology, processed the data, and performed the analysis; KW and JG contributed to data Curation and visualization; SX and JZ wrote the original draft, which was supervised and critically revised by WX. SG, VM, TTW, and LT revised the draft; All authors contributed to the review and editing of the final manuscript.

Declaration of interests

The authors declare that they have no known competing financial interests.

References

1. Abbas, S., Saqib, N., and Shahzad, U.: Global export flow of chilean copper: The role of environmental innovation and renewable energy transition, Geoscience Frontiers, 15, 101697, https://doi.org/10.1016/j.gsf.2023.101697, 2024.
2. Boldy, R., Santini, T., Annandale, M., Erskine, P. D., and Sonter, L. J.: Understanding the impacts of mining on ecosystem services through a systematic review, The Extractive Industries and Society, 8, 457–466, https://doi.org/10.1016/j.exis.2020.12.005, 2021.
3. Carr-Wilson, S., Pattanayak, S. K., and Weinthal, E.: Critical mineral mining in the energy transition: A systematic review of environmental, social, and governance risks and opportunities, Energy Research & Social Science, 116, 103672, https://doi.org/10.1016/j.erss.2024.103672, 2024.
4. Chen, F., Zhu, Y., Bi, Y., Yang, Y., Ma, J., and Peng, S.: High-priority actions to improve carbon sequestration potential for mining ecological restoration in China, Engineering, 47, 16–21, https://doi.org/10.1016/j.eng.2024.09.012, 2025a.
5. Chen, W., Chen, L., Wei, Y., Ruan, L., Fu, Y., Li, W., He, T., and Xiao, W.: Using the forel-ule index (FUI) to track the water quality of subsidence water bodies across the life cycle of coal mining in eastern China, Journal of Environmental Management, 374, 124037, https://doi.org/10.1016/j.jenvman.2025.124037, 2025b.
6. Cook-Patton, S. C., Leavitt, S. M., Gibbs, D., Harris, N. L., Lister, K., Anderson-Teixeira, K. J., Briggs, R. D., Chazdon, R. L., Crowther, T. W., Ellis, P. W., Griscom, H. P., Herrmann, V., Holl, K. D., Houghton, R. A., Larrosa, C., Lomax, G., Lucas, R., Madsen, P., Malhi, Y., Paquette, A., Parker, J. D., Paul, K., Routh, D., Roxburgh, S., Saatchi, S., van den Hoogen, J., Walker, W. S., Wheeler, C. E., Wood, S. A., Xu, L., and Griscom, B. W.: Mapping carbon accumulation potential from global natural forest regrowth, Nature, 585, 545–550, https://doi.org/10.1038/s41586-020-2686-x, 2020.
7. Feng, Y., Zeng, Z., Searchinger, T. D., Ziegler, A. D., Wu, J., Wang, D., He, X., Elsen, P. R., Ciais, P., Xu, R., Guo, Z., Peng, L., Tao, Y., Spracklen, D. V., Holden,

https://doi.org/10.5194/essd-2025-583
Preprint. Discussion started: 12 November 2025

J., Liu, X., Zheng, Y., Xu, P., Chen, J., Jiang, X., Song, X.-P., Lakshmi, V., Wood, E. F., and Zheng, C.: Doubling of annual forest carbon loss over the tropics during the early twenty-first century, Nat Sustain, 5, 444–451, https://doi.org/10.1038/s41893-022-00854-3, 2022.

8. Firozjaei, M. K., Sedighi, A., Firozjaei, H. K., Kiavarz, M., Homaee, M., Arsanjani, J. J., Makki, M., Naimi, B., and Alavipanah, S. K.: A historical and future impact assessment of mining activities on surface biophysical characteristics change: A remote sensing-based approach, Ecol. Indic., 122, 107264, https://doi.org/10.1016/j.ecolind.2020.107264, 2021.
9. Giam, X., Olden, J. D., and Simberloff, D.: Impact of coal mining on stream biodiversity in the US and its regulatory implications, Nat Sustain, 1, 176–183, https://doi.org/10.1038/s41893-018-0048-6, 2018.
10. Giljum, S., Maus, V., Kuschnig, N., Luckeneder, S., Tost, M., Sonter, L. J., and Bebbington, A. J.: A pantropical assessment of deforestation caused by industrial mining, Proceedings of the National Academy of Sciences, 119, e2118273119, https://doi.org/10.1073/pnas.2118273119, 2022.
11. Giljum, S., Maus, V., Sonter, L., Luckeneder, S., Werner, T., Lutter, S., Gershenzon, J., Cole, M. J., Siqueira-Gay, J., and Bebbington, A.: Metal mining is a global driver of environmental change, Nat Rev Earth Environ, 6, 441–455, https://doi.org/10.1038/s43017-025-00683-w, 2025.
12. Gorelick, N., Yang, Z., Arévalo, P., Bullock, E. L., Insfrán, K. P., and Healey, S. P.: A global time series dataset to facilitate forest greenhouse gas reporting, Environ. Res. Lett., 18, 084001, https://doi.org/10.1088/1748-9326/ace2da, 2023.
13. He, T., Zhang, M., Guo, A., Zhai, G., Wu, C., and Xiao, W.: A novel index combining temperature and vegetation conditions for monitoring surface mining disturbance using landsat time series, CATENA, 229, 107235, https://doi.org/10.1016/j.catena.2023.107235, 2023.
14. Hilson, G., Hilson, A., Maconachie, R., McQuilken, J., and Goumandakoye, H.: Artisanal and small-scale mining (ASM) in sub-Saharan Africa: Re-conceptualizing formalization and 'illegal' activity, Geoforum, 83, 80–90, https://doi.org/10.1016/j.geoforum.2017.05.004, 2017.
15. Jacquin, A., Sheeren, D., and Lacombe, J.-P.: Vegetation cover degradation assessment in madagascar savanna based on trend analysis of MODIS NDVI time series, International Journal of Applied Earth Observation and Geoinformation, 12, S3–S10, https://doi.org/10.1016/j.jag.2009.11.004, 2010.
16. Jiang, Y., Liu, S., Liu, M., Peng, X., Liao, X., Wang, Z., and Gao, H.: A systematic framework for continuous monitoring of land use and vegetation dynamics in multiple heterogeneous mine sites, Remote Sens Ecol Conserv, 8, 793–807, https://doi.org/10.1002/rse2.276, 2022a.
17. Jiang, Y., Liu, S., Liu, M., Peng, X., Liao, X., Wang, Z., and Gao, H.: A systematic framework for continuous monitoring of land use and vegetation dynamics in multiple heterogeneous mine sites, Remote Sens Ecol Conserv, 8, 793–807, https://doi.org/10.1002/rse2.276, 2022b.
18. Karan, S. K., Samadder, S. R., and Maiti, S. K.: Assessment of the capability of

remote sensing and GIS techniques for monitoring reclamation success in coal mine degraded lands, Journal of Environmental Management, 182, 272–283, https://doi.org/10.1016/j.jenvman.2016.07.070, 2016.

19. Kennedy, R. E., Yang, Z., and Cohen, W. B.: Detecting trends in forest disturbance and recovery using yearly landsat time series: 1. LandTrendr — temporal segmentation algorithms, Remote Sensing of Environment, 114, 2897–2910, https://doi.org/10.1016/j.rse.2010.07.008, 2010.
20. Ladewig, M., Angelsen, A., Masolele, R. N., and Chervier, C.: Deforestation triggered by artisanal mining in eastern Democratic Republic of the Congo, Nat Sustain, 7, 1452–1460, https://doi.org/10.1038/s41893-024-01421-8, 2024.
21. Li, H., Wang, P., Werner, T. T., Chen, B., and Chen, W.-Q.: Machine learning-enhanced monitoring of global copper mining areas, Sci Data, 12, 1120, https://doi.org/10.1038/s41597-025-05296-y, 2025.
22. Li, S., Xiao, W., Zhao, Y., and Lv, X.: Incorporating ecological risk index in the multi-process MCRE model to optimize the ecological security pattern in a semi-arid area with intensive coal mining: A case study in northern China, Journal of Cleaner Production, 247, 119143, https://doi.org/10.1016/j.jclepro.2019.119143, 2020.
23. Liang, T., Werner, T. T., Heping, X., Jingsong, Y., and Zeming, S.: A global-scale spatial assessment and geodatabase of mine areas, Global and Planetary Change, 204, 103578, https://doi.org/10.1016/j.gloplacha.2021.103578, 2021.
24. Lv, X., Xiao, W., Zhao, Y., Zhang, W., Li, S., and Sun, H.: Drivers of spatio-temporal ecological vulnerability in an arid, coal mining region in western China, Ecological Indicators, 106, 105475, https://doi.org/10.1016/j.ecolind.2019.105475, 2019.
25. Ma, Q., Wu, J., He, C., and Fang, X.: The speed, scale, and environmental and economic impacts of surface coal mining in the Mongolian Plateau, Resources, Conservation and Recycling, 173, 105730, https://doi.org/10.1016/j.resconrec.2021.105730, 2021.
26. Maus, V. and Werner, T. T.: Impacts for half of the world's mining areas are undocumented, Nature, 625, 26–29, https://doi.org/10.1038/d41586-023-04090-3, 2024.
27. Maus, V., Giljum, S., Gutschlhofer, J., Da Silva, D. M., Probst, M., Gass, S. L. B., Luckeneder, S., Lieber, M., and McCallum, I.: A global-scale data set of mining areas, Sci Data, 7, 289, https://doi.org/10.1038/s41597-020-00624-w, 2020.
28. Maus, V., Giljum, S., da Silva, D. M., Gutschlhofer, J., da Rosa, R. P., Luckeneder, S., Gass, S. L. B., Lieber, M., and McCallum, I.: An update on global mining land use, Sci Data, 9, 433, https://doi.org/10.1038/s41597-022-01547-4, 2022.
29. McKenna, P. B., Lechner, A. M., Phinn, S., and Erskine, P. D.: Remote sensing of mine site rehabilitation for ecological outcomes: A global systematic review, Remote Sensing, 12, 3535, https://doi.org/10.3390/rs12213535, 2020.
30. Mi, J., Yang, Y., Zhang, S., An, S., Hou, H., Hua, Y., and Chen, F.: Tracking the Land Use/Land Cover Change in an Area with Underground Mining and Reforestation via Continuous Landsat Classification, Remote Sensing, 11, 1719,

https://doi.org/10.5194/essd-2025-583
Preprint. Discussion started: 12 November 2025

https://doi.org/10.3390/rs11141719, 2019.

31. Murguía, D. I. and Bringezu, S.: Measuring the specific land requirements of large-scale metal mines for iron, bauxite, copper, gold and silver, PIE, 10, 264, https://doi.org/10.1504/PIE.2016.082142, 2016.
32. Olson, D. M., Dinerstein, E., Wikramanayake, E. D., Burgess, N. D., Powell, G. V. N., Underwood, E. C., D'amico, J. A., Itoua, I., Strand, H. E., Morrison, J. C., Loucks, C. J., Allnutt, T. F., Ricketts, T. H., Kura, Y., Lamoreux, J. F., Wettengel, W. W., Hedao, P., and Kassem, K. R.: Terrestrial ecoregions of the world: A new map of life on earth: a new global map of terrestrial ecoregions provides an innovative tool for conserving biodiversity, BioScience, 51, 933–938, https://doi.org/10.1641/0006-3568(2001)051[0933:TEOTWA]2.0.CO;2, 2001.
33. Oramah, I. T., Richards, J. P., Summers, R., Garvin, T., and McGee, T.: Artisanal and small-scale mining in Nigeria: Experiences from Niger, Nasarawa and Plateau states, The Extractive Industries and Society, 2, 694–703, https://doi.org/10.1016/j.exis.2015.08.009, 2015.
34. Pavloudakis, F., Roumpos, C., and Spanidis, P.-M.: Sustainable Mining and Processing of Mineral Resources, Sustainability, 16, 8393, https://doi.org/10.3390/su16198393, 2024.
35. Poorter, L., Craven, D., Jakovac, C. C., van der Sande, M. T., Amissah, L., Bongers, F., Chazdon, R. L., Farrior, C. E., Kambach, S., Meave, J. A., Muñoz, R., Norden, N., Rüger, N., van Breugel, M., Almeyda Zambrano, A. M., Amani, B., Andrade, J. L., Brancalion, P. H. S., Broadbent, E. N., de Foresta, H., Dent, D. H., Derroire, G., DeWalt, S. J., Dupuy, J. M., Durán, S. M., Fantini, A. C., Finegan, B., Hernández-Jaramillo, A., Hernández-Stefanoni, J. L., Hietz, P., Junqueira, A. B., N'dja, J. K., Letcher, S. G., Lohbeck, M., López-Camacho, R., Martínez-Ramos, M., Melo, F. P. L., Mora, F., Müller, S. C., N'Guessan, A. E., Oberleitner, F., Ortiz-Malavassi, E., Pérez-García, E. A., Pinho, B. X., Piotto, D., Powers, J. S., Rodríguez-Buriticá, S., Rozendaal, D. M. A., Ruíz, J., Tabarelli, M., Teixeira, H. M., Valadares de Sá Barretto Sampaio, E., van der Wal, H., Villa, P. M., Fernandes, G. W., Santos, B. A., Aguilar-Cano, J., de Almeida-Cortez, J. S., Alvarez-Davila, E., Arreola-Villa, F., Balvanera, P., Becknell, J. M., Cabral, G. A. L., Castellanos-Castro, C., de Jong, B. H. J., Nieto, J. E., Espírito-Santo, M. M., Fandino, M. C., García, H., García-Villalobos, D., Hall, J. S., Idárraga, A., Jiménez-Montoya, J., Kennard, D., Marín-Spiotta, E., Mesquita, R., Nunes, Y. R. F., Ochoa-Gaona, S., Peña-Claros, M., Pérez-Cárdenas, N., Rodríguez-Velázquez, J., Villanueva, L. S., Schwartz, N. B., Steininger, M. K., Veloso, M. D. M., Vester, H. F. M., Vieira, I. C. G., Williamson, G. B., Zanini, K., and Hérault, B.: Multidimensional tropical forest recovery, Science, 374, 1370–1376, https://doi.org/10.1126/science.abh3629, 2021.
36. Qian, D., Yan, C., Xiu, L., and Feng, K.: The impact of mining changes on surrounding lands and ecosystem service value in the Southern Slope of Qilian Mountains, Ecological Complexity, 36, 138–148, https://doi.org/10.1016/j.ecocom.2018.08.002, 2018.
37. Ross, M. L. and Werker, E.: Diversification in resource-rich africa, 1999–2019, Resources Policy, 88, 104437, https://doi.org/10.1016/j.resourpol.2023.104437,

2024.
38. Sonter, L. J., Herrera, D., Barrett, D. J., Galford, G. L., Moran, C. J., and Soares-Filho, B. S.: Mining drives extensive deforestation in the Brazilian Amazon, Nat Commun, 8, 1013, https://doi.org/10.1038/s41467-017-00557-w, 2017.
39. Sonter, L. J., Ali, S. H., and Watson, J. E. M.: Mining and biodiversity: Key issues and research needs in conservation science, Proc. R. Soc. B., 285, https://doi.org/10.1098/rspb.2018.1926, 2018.
40. Sonter, L. J., Nursamsi, I., Bennun, L., Graham, J., Maus, V., Rainey, H., Starkey, M., Turner, J. A., Watson, J. E. M., and Prescott, G. W.: Global land cover maps do not reveal mining pressures to biodiversity, Sci Rep, 15, 22421, https://doi.org/10.1038/s41598-025-01959-3, 2025.
41. Tai, X., Xiao, W., and Tang, Y.: A quantitative assessment of vulnerability using social-economic-natural compound ecosystem framework in coal mining cities, Journal of Cleaner Production, 258, 120969, https://doi.org/10.1016/j.jclepro.2020.120969, 2020.
42. Tang, L. and Werner, T. T.: Global mining footprint mapped from high-resolution satellite imagery, Commun Earth Environ, 4, 134, https://doi.org/10.1038/s43247-023-00805-6, 2023.
43. Werner, T. T., Bebbington, A., and Gregory, G.: Assessing impacts of mining: Recent contributions from GIS and remote sensing, The Extractive Industries and Society, 6, 993–1012, https://doi.org/10.1016/j.exis.2019.06.011, 2019.
44. Werner, T. T., Mudd, G. M., Schipper, A. M., Huijbregts, M. A. J., Taneja, L., and Northey, S. A.: Global-scale remote sensing of mine areas and analysis of factors explaining their extent, Global Environmental Change, 60, 102007, https://doi.org/10.1016/j.gloenvcha.2019.102007, 2020.
45. Xiang, H., Wang, Z., Mao, D., Zhang, J., Zhao, D., Zeng, Y., and Wu, B.: Surface mining caused multiple ecosystem service losses in China, Journal of Environmental Management, 290, 112618, https://doi.org/10.1016/j.jenvman.2021.112618, 2021.
46. Xiao, W., Lv, X., Zhao, Y., Sun, H., and Li, J.: Ecological resilience assessment of an arid coal mining area using index of entropy and linear weighted analysis: A case study of shendong coalfield, China, Ecological Indicators, 109, 105843, https://doi.org/10.1016/j.ecolind.2019.105843, 2020a.
47. Xiao, W., Deng, X., He, T., and Chen, W.: Mapping annual land disturbance and reclamation in a surface coal mining region using google earth engine and the LandTrendr algorithm: A case study of the shengli coalfield in inner mongolia, China, Remote Sensing, 12, 1612, https://doi.org/10.3390/rs12101612, 2020b.
48. Xiao, W., Deng, X., He, T., and Chen, W.: Mapping annual land disturbance and reclamation in a surface coal mining region using google earth engine and the LandTrendr algorithm: A case study of the shengli coalfield in inner mongolia, China, Remote Sensing, 12, 1612, https://doi.org/10.3390/rs12101612, 2020c.
49. Xu, H., Xu, F., Lin, T., Xu, Q., Yu, P., Wang, C., Aili, A., Zhao, X., Zhao, W., Zhang, P., Yang, Y., and Yuan, K.: A systematic review and comprehensive analysis on ecological restoration of mining areas in the arid region of China: Challenge,

capability and reconsideration, Ecol. Indic., 154, 110630, https://doi.org/10.1016/j.ecolind.2023.110630, 2023.

50. Xu, S., Zhou, J., and Xiao, W.: Global surface mining and land reclamation of time series from 1985–2022, https://doi.org/10.5281/ZENODO.17085099, 2025.
51. Yan, X., Li, J., Shao, Y., Ma, T., Zhang, R., and Su, Y.: Assessing open-pit mining impacts on semi-arid grassland: A framework for boundary and intensity quantification, J. Cleaner Prod., 475, 143464, https://doi.org/10.1016/j.jclepro.2024.143464, 2024.
52. Yang, Y., Erskine, P. D., Lechner, A. M., Mulligan, D., Zhang, S., and Wang, Z.: Detecting the dynamics of vegetation disturbance and recovery in surface mining area via landsat imagery and LandTrendr algorithm, Journal of Cleaner Production, 178, 353–362, https://doi.org/10.1016/j.jclepro.2018.01.050, 2018.
53. Yonk, R. M., Smith, J. T., and Wardle, A. R.: Exploring the policy implications of the surface mining control and reclamation act, Resources, 8, 25, https://doi.org/10.3390/resources8010025, 2019.
54. Yu, L., Xu, Y., Xue, Y., Li, X., Cheng, Y., Liu, X., Porwal, A., Holden, E.-J., Yang, J., and Gong, P.: Monitoring surface mining belts using multiple remote sensing datasets: A global perspective, Ore Geology Reviews, 101, 675–687, https://doi.org/10.1016/j.oregeorev.2018.08.019, 2018.
55. Zhang, X., Zhao, T., Xu, H., Liu, W., Wang, J., Chen, X., and Liu, L.: GLC_FCS30D: the first global 30 m land-cover dynamics monitoring product with a fine classification system for the period from 1985 to 2022 generated using dense-time-series Landsat imagery and the continuous change-detection method, Earth Syst. Sci. Data, 16, 1353–1381, https://doi.org/10.5194/essd-16-1353-2024, 2024.
56. Zhao, Y., Wang, Y., Zhang, Z., Zhou, Y., Huang, H., and Chang, M.: The Evolution of Landscape Patterns and Its Ecological Effects of Open-Pit Mining: A Case Study in the Heidaigou Mining Area, China, Int. J. Environ. Res. Public. Health, 20, 4394, https://doi.org/10.3390/ijerph20054394, 2023.